MATERIALS SCIENCE

Meter-scale van der Waals films manufactured via one-step roll printing

Kyuho Lee[1,2,3]†, Naoki Higashitarumizu[1,2,4]†, Shu Wang[2,5], Chunghee Kim[1,2,6], Chun Yuen Ho[1,2,7], Jin Woo Oh[3], Guangtao Zan[3], Morten Madsen[7,8], Tae-Woo Lee[6,9], Daryl C. Chrzan[2,5], Cheolmin Park[3]*, Ali Javey[1,2]*

A weak van der Waals (vdW) force in layered materials enables their isolation into thin flakes through mechanical exfoliation while sustaining their intrinsic electronic and optical properties. Here, we introduce a universal roll-printing method capable of producing vdW multilayer films on wafer-to-meter scale. This process uses sequential exfoliation and transfer of layered materials from the powder sources to target substrates through a repeated rolling of a cylindrical metal drum. We achieve uniformly coated films with a library of vdW powders on various mechanically rigid and flexible substrates. The printed films are configured into different devices including light-emitting diodes and photodetectors. The presented technique offers substantial benefits in terms of cost efficiency and a low thermal budget while offering high material quality.

INTRODUCTION

Van der Waals (vdW) two-dimensional (2D) materials have been widely explored for diverse applications. Notable advancements have been achieved using chemical vapor deposition for large-area synthesis of mono-to-few layer films (*1*–*5*). Recently, multilayers of certain vdW materials have garnered considerable interest with their distinctive optoelectronic, electrical, and/or thermal properties at the "bulk" thicknesses (*6*–*10*). These multilayer vdW materials are promising for applications such as mid-infrared (IR) to visible light emitters and detectors, batteries, electromagnetic shielding, and catalysis (*8*–*14*). In this regard, the development of a scalable and generic fabrication process that is compatible with different substrates, including those with low thermal budget, is of profound interest.

Here, we present a roll-printing technique for wafer-to-meter-scale production of vdW multilayer films. Leveraging the weak vdW interlayer forces, our simple method enables direct sequential exfoliation and transfer of layered materials from powders to substrates through a repetitive rolling process. The use of a lubricant facilitates the formation of uniform films. The process is performed at room temperature (RT), making it compatible with a wide range of substrates, including paper, plastics, quartz, and silicon. The roll-printed films exhibit excellent optoelectronic performance because the highest-quality vdW materials, available today in the form of bulk crystals, are assembled seamlessly in a multilayer form without solution processing. As an example, we demonstrate wafer-scale black phosphorus (BP) films, exhibiting a luminescence quantum yield comparable to that of its bulk crystal and exceeding that of conventional III-V and II-VI semiconductors with similar mid-IR bandgaps. We also show the process's compatibility with different vdW semiconductors, insulators, and conductors. In one application, BP, phosphorus-arsenic ($P_{1-x}As_x$) alloys, InSe, and ReS_2 films on plastic substrates are used as phosphors in mid-IR to visible wavelengths for selective gas sensing. With a standard device fabrication processes, various electronic and optoelectronic devices are fabricated, including light-emitting diodes (LEDs) and detectors.

RESULTS AND DISCUSSION

2D layered materials have been used through various exfoliation methods, including mechanical exfoliation (*15*, *16*), electrochemical exfoliation (*17*, *18*), intercalation (*19*, *20*), and liquid exfoliation (*21*–*25*). All these processes take advantage of the weak interlayer forces compared to strong in-plane covalent bonding of vdW materials. Here, we devise a universal roll-printing process for the direct formation of vdW films on a variety of substrates. Figure 1A presents a schematic illustration of the roll-printing setup. The target substrate was partially covered with vdW powders (0.6 mg/cm^2); then, a 2.5-μl mixture of octane and mineral oil (2:1 volume ratio) was applied as a lubricant (*26*, *27*). A cylindrical stainless-steel rod was repeatedly rolled back and forth on the sample at RT with an applied normal force of 20 N. The lubricant facilitates the movement and rearrangement of microparticles at the roller/substrate interface for improved exfoliation and transfer, and it prevents scratching of the assembled film. Movies S1 and S2 show the rolling process with and without the use of lubricant, respectively: A continuous film was achieved with lubricant, while an uneven film was formed without it. As an example, this method was used for thin film processing of BP on a 100-mm Si wafer (Fig. 1B). Cross-sectional scanning electron microscopy (SEM) and energy-dispersive x-ray spectroscopy (EDS) mapping were performed for the roll-printed BP film as shown in Fig. 1 (C and D), respectively. Figure S1 shows the thickness distribution of each flake forming the 2-μm-thick BP film. The median flake thickness was 90 nm, which is reasonably thin to achieve a uniform film with a total thickness of micrometers, while a wide thickness distribution was obtained from ~10 nm to 1 μm.

[1]Electrical Engineering and Computer Sciences, University of California, Berkeley, CA 94720, USA. [2]Materials Sciences Division, Lawrence Berkeley National Laboratory, Berkeley, CA 94720, USA. [3]Department of Materials Science and Engineering, Yonsei University, Seoul, 03722, Republic of Korea. [4]JST, PRESTO, 4-1-8 Honcho, Kawaguchi, Saitama 332-0012, Japan. [5]Materials Science and Engineering, University of California, Berkeley, CA 94720, USA. [6]Department of Materials Science and Engineering, Seoul National University, Seoul 08826, Republic of Korea. [7]Center for Advanced Photovoltaics and Thin Film Energy Devices (SDU CAPE), Mads Clausen Institute, University of Southern Denmark, 6400 Sønderborg, Denmark. [8]SDU Climate Cluster, University of Southern Denmark, Odense 5230, Denmark. [9]Research Institute of Advanced Materials, Institute of Engineering Research, Seoul National University, Seoul 08826, Republic of Korea.
*Corresponding author. Email: ajavey@berkeley.edu (A.J.); cmpark@yonsei.ac.kr (C.P.)
†These authors contributed equally to this work.

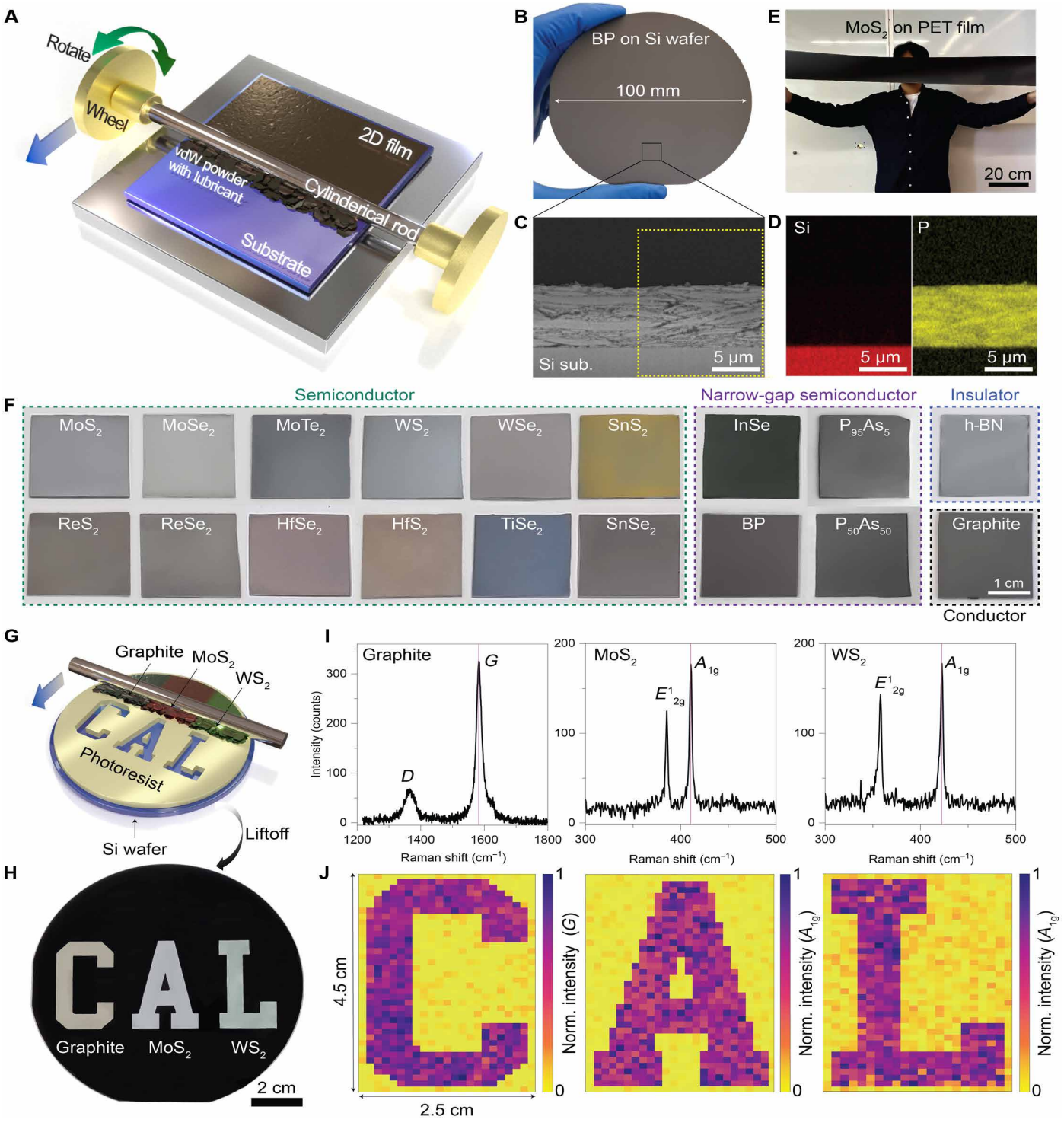

Fig. 1. Wafer-scale roll-printing method for vdW materials. (**A**) Schematic illustration of roll-printing setup. (**B**) Photographs of BP film on a 100-mm Si wafer. (**C**) Cross-sectional SEM image and (**D**) EDS mapping of the BP film on Si wafer. (**E**) MoS_2 film on a PET substrate fabricated by the roll-printing method. (**F**) Photographs of various vdW material films on Si wafers. (**G**) Schematic illustration for printing CAL with graphite, MoS_2, and WS_2 powders on a patterned photoresist and (**H**) a photograph of CAL on a 100-mm Si wafer after the liftoff process. (**I**) Raman spectra of graphite, MoS_2, and WS_2 films. (**J**) Spatial mapping of normalized Raman intensity for patterned graphite "C", MoS_2 "A", and WS_2 "L": I (G) at 1580 cm^{-1}, I (A_{1g}) at 410 cm^{-1}, and I (A_{1g}) at 422 cm^{-1}, respectively. Raman mapping was performed with 100-μm spatial step on a ~2.5 cm-by-4.5 cm area.

This uneven flake thickness was due to the difficulty of thinning down relatively thick flakes once they are embedded inside the film. To achieve further flake thickness uniformity, prescreening of vdW particle size via filtration before rolling can be considered. By rearranging particles during the rolling process, the BP flakes aligned along the substrate rather than standing vertically. The process was scaled up to meter-long substrates (Fig. 1E) for MoS_2 on a polyethylene terephthalate (PET) sheet (over 2000 cm^2). As the process is performed at RT, it is compatible with various substrates, including silicon, glass, quartz, and diverse polymeric substrates, and is generic for different vdW materials such as BP, $P_{1-x}As_x$ alloys, WS_2, WSe_2, MoS_2, $MoSe_2$, $MoTe_2$, SnS_2, $SnSe_2$, $ReSe_2$, ReS_2, InSe, $HfSe_2$, HfS_2, hexagonal boron nitride (h-BN), and graphite (Fig. 1F and fig. S2). The exfoliation was successful by rolling process for BP and its alloys, which has relatively high interlayer binding energy (33.4 meV $Å^{-2}$) compared to graphite, h-BN, and transition metal dichalcogenides whose interlayer binding energy is 18.8 to 26.3 meV $Å^{-2}$ (*16*). The film thickness can be controlled from 0.8 to 6.0 μm by adjusting the amount of powder, the number of repeated rolling cycles, and the magnitude of normal force (fig. S3). The roll-printed films were mechanically stable on the substrate. For the roll-printed graphite film on PET substrate, a stable sheet resistance was confirmed through repeated bending up to 3000 cycles without film delamination or degradation (fig. S4). This mechanical robustness enabled film patterning using a patterned photoresist before the rolling process. As an example, we used photolithography to pattern the photoresist with "CAL" on a Si wafer and subsequently roll-printed graphite, MoS_2, and WS_2 onto the "C," "A," and "L" patterns, respectively (Fig. 1G). Moreover, we demonstrated micropatterned WS_2/MoS_2 lines and space with widths of 15 and 5 μm, respectively (fig. S5). For finer resolution and pitch, more efforts can be made to decrease the initial size of vdW particles. In addition, post-rolling patterning via reactive ion etching can be useful for obtaining steep pattern edges. After thermal annealing at 80°C, the photoresist was removed by liftoff in acetone, leaving behind the CAL pattern with different vdW materials, as shown in Fig. 1H. Figure 1 (I and J) shows the Raman spectra and mapping of the patterned graphite, MoS_2, and WS_2 films. Clear peaks were found at around 1580, 410, and 422 cm^{-1} for G-mode in graphite, A_{1g} mode in MoS_2, and A_{1g} mode in WS_2, respectively. The Raman mapping data reveals distinct Raman peaks, indicating the preserved crystalline quality during the roll-printing processes.

The mechanism of the roll-printing process is illustrated in Fig. 2A. The passage of the roller creates a substantial shear force that cause the particles to fracture. These fractures are primarily interlayer, as the interlayer bonds are inherently weaker than the intralayer covalent bonds of the 2D particles. Through this process, the powder particles become more "plate-like." The normal force exerted by the roller induces some particles to bond to the substrate, while others bond to the roller or remain in the lubricant. The particles bonded to the roller are then available for deposition in other regions of the substrate. Through repeated back-and-forth rolling, sequential exfoliation and transfer of the vdW flakes occur between the roller and the substrate, ultimately leading to the formation of a flat film on both the substrate and the roller (fig. S6). The lubricant facilitates the rearrangement of particles at the roller/substrate interface and helps to sweep away excess vdW particles during each rolling step without scratching the formed thin film. To remove the residual lubricant from the film, the sample is rinsed in isopropyl alcohol (IPA) and then subjected to vacuum annealing at 100°C, as schematically illustrated in Fig. 2A (iii and iv).

Figure 2B presents the results of a Fourier transform IR (FT-IR) spectroscopy comparative analysis of the BP films after fabrication and after undergoing IPA rinsing and vacuum annealing, as compared

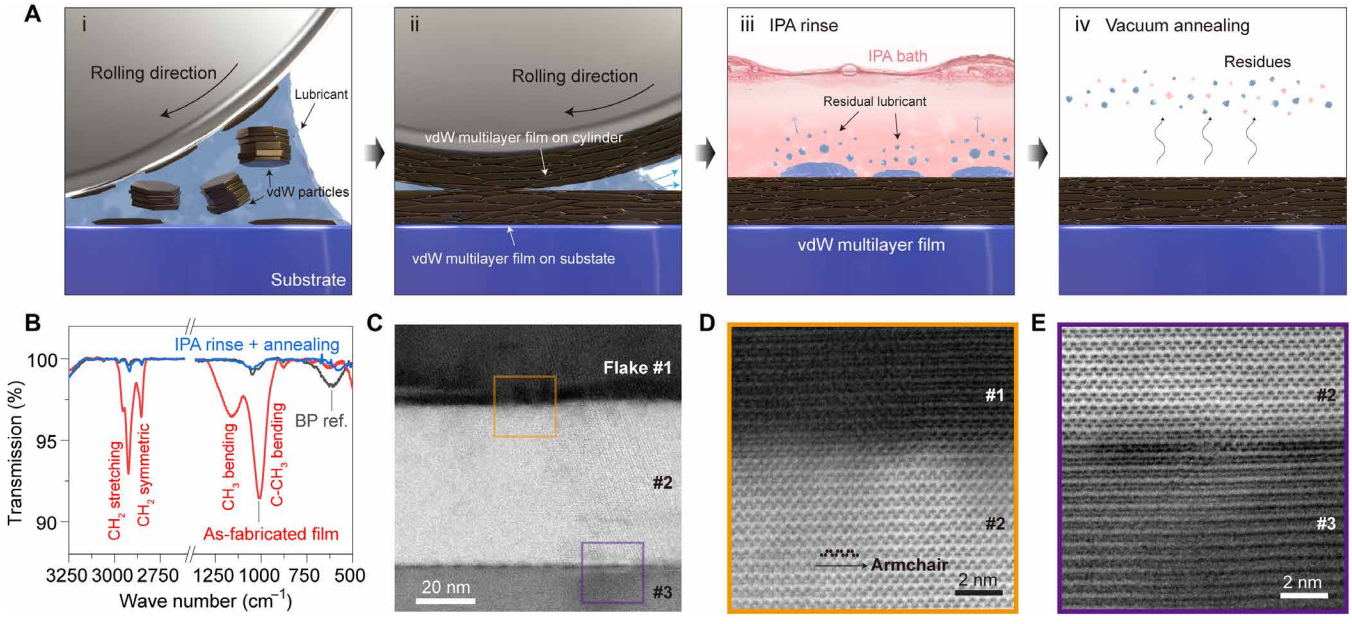

Fig. 2. Mechanism of roll printing. (**A**) Schematic illustration of roll-printing process and the post-treatments for the removal of residual lubricant by isopropyl alcohol (IPA) rinsing and vacuum annealing. (**B**) Fourier transform IR (FTIR) spectroscopy analysis of bulk BP source, as-fabricated roll-printed BP film, and the BP film after IPA rinsing with vacuum annealing. (**C**) Cross-sectional scanning transmission electron microscopy (STEM) image of BP film. High-angle annular dark-field (HAADF)–STEM images of the interfaces between (**D**) flakes 1 and 2 and (**E**) flakes 2 and 3.

with the pristine bulk BP powder. This analysis distinctly illustrates the effective removal of the lubricant after the IPA rinsing and vacuum annealing, as evidenced by the substantial reduction of CH_2, CH_3, and C-CH_3–related transmission peaks. To ascertain the dense arrangement of BP flakes and their interfaces within the film, detailed analyses were carried out using high-resolution scanning transmission electron microscopy (STEM). In Fig. 2C, multiple BP flakes stacked vertically can be observed. High-resolution high-angle annular dark-field (HAADF)–STEM images were taken at the interfaces, specifically between flake 1 and flake 2 (highlighted in an orange box) and between flake 2 and flake 3 (marked by a purple box). The steep interfaces were locally confirmed in the HAADF-STEM images (Fig. 2, D and E), while void formations were partially confirmed in randomly selected spots over the entire film (fig. S7), as well as large-area SEM images (Fig. 1C). These voids could possibly be caused by the sample preparation processes, such as focused ion beams and ion beam cross-sectional polisher process for TEM and SEM, respectively; however, it cannot be excluded that the voids were formed during the rolling process. Further optimization of the rolling process could minimize voids and disorders, leading to higher-quality films and improved device performance. The difference in contrast of cross-sectional images for each flake is possibly due to the variation of the flake's lateral size, causing the varied measured depth along the in-plane direction. The flakes exhibit different crystal orientations, as shown in the high-resolution TEM image (fig. S8A). The change in crystal orientation across the border was also confirmed by the selected-area electron diffraction pattern (fig. S8B).

To further study the properties of roll-printed films, we performed x-ray diffraction (XRD) and x-ray photoelectron spectroscopy (XPS) of a BP film on a 100-mm quartz wafer, roll-printed inside of a nitrogen glovebox (Fig. 3A). The XRD data revealed a crystal orientation of (0 2 0), attributed to the alignment of BP flakes along the rolling direction, as shown in Fig. 3B. This property was maintained over a centimeter scale with high uniformity, as confirmed by the XRD mapping (Fig. 3C). High-resolution XPS spectra at P 2p core energy is depicted in Fig. 3D. The phosphorus P 2p photoelectron spectrum exhibits the spin-orbital splitting doublet located at 130.4 eV ($2p_{3/2}$) and 131.3 eV ($2p_{1/2}$), which are characteristic of crystalline BP (*28*). Phosphorus oxides could be detected as

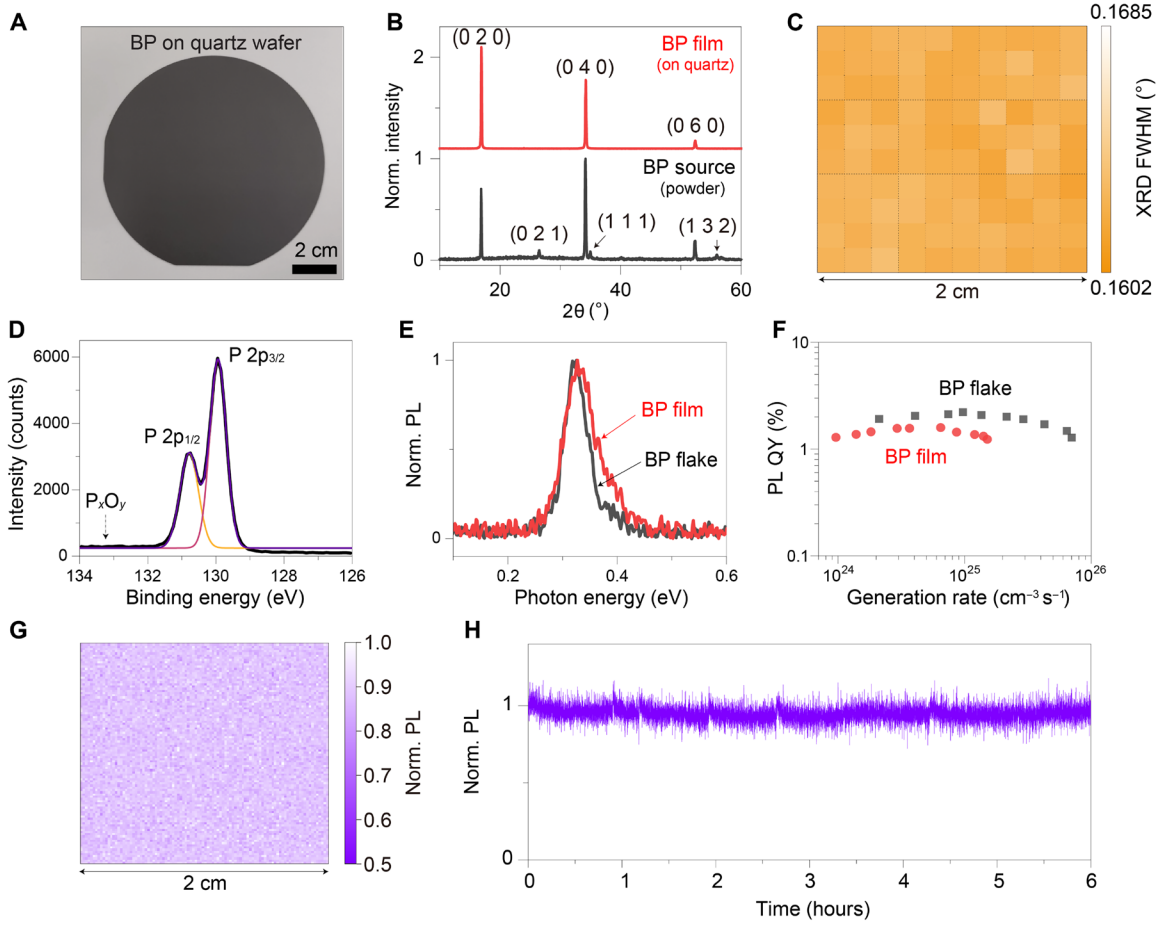

Fig. 3. Optical and crystallographic characterizations of large-area BP film. (**A**) Photograph of BP film on 100-mm quartz wafer. (**B**) X-ray diffraction (XRD) data of BP film on quartz wafer and BP source powder. (**C**) Spatial mapping of full width at half maximum (FWHM) of (0 2 0) plane peak for 2 cm–by–2 cm area with a step size of 2 mm. (**D**) X-ray photoelectron spectroscopy (XPS) results of BP film. (**E**) Normalized photoluminescence (PL) spectra of exfoliated BP flake and roll-printed BP film. (**F**) PL quantum yield (QY) of BP film as a function of generation rate, compared with that of the mechanically exfoliated BP flake. (**G**) Normalized PL intensity map measured on an area of 2 cm by 2 cm with a step size of 200 μm. (**H**) Time-resolved measurement of PL for 6 hours at a pump power of 7.0 mW (638-nm wavelength) in air.

photoemission peaks in the range of 132 to 136 eV. However, no such peaks were found in the BP film.

The quality of films can be more comprehensively investigated using photoluminescence (PL) spectroscopy, which is more sensitive to defects and impurities than crystallographic characterizations such as Raman and XRD measurements. Notably, BP remains direct bandgap from bulk thickness to ~10 layers to show PL in mid-IR wavelength (*9*). Figure 3E shows the typical PL spectra for both exfoliated BP flake (600 nm thick) and roll-printed BP film (1 μm thick). For the roll-printed BP film, the peak emission wavelength appeared at 0.33 eV consistent with its intrinsic bandgap at the bulk thickness limit. When the normal force was varied between 5 and 50 N, no significant change was observed in the PL intensity and spectrum shape (fig. S9). This is likely due to the tightly stacked flakes maintaining vdW contact even at lower normal forces, as seen in the cross-sectional TEM images (Fig. 2, C to E). We conducted a calibrated PL quantum yield (QY) measurement on the roll-printed BP film (detailed in Materials and Methods). Figure 3F shows the PL QY of a 1-μm-thick BP film as a function of the generation rate, and, for comparison, that of exfoliated BP flake (600 nm thick) is also presented. The BP film shows comparable PL QY to that of exfoliated BP flake, depicting the high optoelectronic quality of the roll-printed films. Notably, the vdW interfaces of the stacked flakes have minimal effect on non-radiative recombination losses due to the inherently self-terminated surfaces of 2D materials. Figure 3G shows the color mapping of the PL intensity at the generation rate of 5×10^{24} cm^{-3} s^{-1} measured in ambient air. Uniform PL emission was observed across a centimeter scale. The PL intensity remained unchanged after 6 hours of continuous measurements, depicting the stability of the films (Fig. 3H).

Stable and bright emitter in IR is in demand for various emerging applications, including gas sensing, where molecules can be identified by their distinct absorption characteristics. As a proof of concept, we used roll-printed films as a phosphor for nondispersive IR (NDIR) gas sensing. Figure 4A shows the schematic of NDIR gas-sensing setup. An external laser was used to optically excite the vdW thin film, directing its emission into a gas chamber. Band-pass filters were used to allow a specific IR wavelength to pass selectively, corresponding to each gas's absorption band. The 1-μm-thick vdW films were fabricated on plastic disks attached to a rotating wheel (Fig. 4B). Multiple emission wavelengths were obtained by using direct bandgap vdW materials, including BP, $P_{1-x}As_x$, InSe, and ReS_2. Figure 4C depicts the normalized PL spectra of these roll-printed films as measured by both visible/near-IR spectrometers and FTIR systems (further details in Materials and Methods). With optical excitation from the 638-nm laser, we accomplished a broad emission range from of ~0.27 to 1.5 eV. A comparison of PL intensity of roll-printed films and their bulk sources is shown in fig. S10. For BP and BPAs sources, we confirmed several-fold reductions in PL intensity, which can be caused by the enhanced non-radiative recombination with process-induced defect states at the flake edges (*29*). Note that these phosphors can facilitate a multiplexed wavelength system via a singular visible light source, eliminating the need for metal contacts, p-n junctions, or other complex device structures. In particular, in the mid-IR wavelength, gas molecules exhibit intrinsic light absorption, based on their vibrational and rotational energy states. Figures 4 (D and F) displays the phosphor emission spectra from $P_{50}As_{50}$ and the BP films for CO_2 and CH_4 detection, respectively. The $P_{50}As_{50}$ emission exhibited a large overlap with the CO_2 absorption band, traced in the emission spectrum around 4.3 μm (Fig. 4D). In contrast, CH_4 absorption was detected in the BP's emission spectrum near 3.3 μm (Fig. 4F). For practical use, a high-speed response together with stability is crucial for precise gas concentration measurements. To evaluate the present phosphor's emission performance, time resolved absorption measurement was conducted. Figure 4E shows the normalized emission intensity of the $P_{50}As_{50}$ film at varying CO_2 concentrations. Introduction of CO_2 gas and N_2 purging gas exhibited a marked response, with consistent emission amplitude. A similar response was verified during CH_4 detection with BP film (Fig. 4G). The light absorption dependence on the gas concentration adheres to the exponential attenuation with depth, as dictated by the Beer-Lambert law model

$$I = \exp(-kLx) \quad (1)$$

where k is a fitting function, L is the chamber length (75 mm), and x stands for the gas concentration. The experimental results, detecting IR intensity in relation to the target gas concentration, aligned with the exponential model (inset in Fig. 4, E and G).

Electrically injected micro-LEDs using 1.5 μm-thick BP printed films were also fabricated. Figure 5A outlines the device structure. The zinc oxide (ZnO)/BP/poly(3,4-ethylenedioxythiophene)-poly(styrenesulfonate) (PEDOT:PSS) heterolayers were processed on a gold bottom contact, followed by deposition of an indium tin oxide (ITO) layer via sputtering, which served as a transparent top contact electrode (additional details in Materials and Methods). We designed a 4 × 4 pixel array on a SiO_2/Si substrate, where the bottom Au electrode was fashioned to operate each LED individually (see Fig. 5B). The PEDOT:PSS and the ZnO nanoparticle films were spin-coated to serve as hole and electron injection layer, respectively (see Fig. 5C). Figure 5D shows the I_D-V_D curves of 16 BP-based LEDs. The device-to-device variation of the forward bias resistance is 6.0% (SD). The electroluminescence (EL) characteristics were investigated, and the spectra at different injection currents are plotted in Fig. 5E. The peak emission is at 0.32 eV, which is consistent with the PL spectra (Fig. 3E). As indicated in Fig. 5F, each LED pixel's performance remained within the variation of 6.0% (SD) (fig. S11). Figure S12 shows the height profile mapping of roll-printed BP film. The variation of local thickness over the entire film may result in device-to-device variation of EL efficiency (Fig. 5, D and F). Given that current vdW films can be patterned using standard lithography (as shown in Fig. 1, G and H), different materials can be arranged into a multipixel array to achieve multiple colors.

In another device demonstration, we fabricated photoconductor pixel arrays based on a roll-printed WS_2 film. The process entailed patterning a photoresist on a SiO_2/Si substrate using standard photolithography, followed by a roll printing of WS_2 film (~2 μm thickness) and liftoff, resulting in a 500 μm–by–500 μm pixel array (Fig. 6A). Film thickness was able to be controlled by using different thickness photoresist templates. Figure S13 shows height profiles for patterned WS_2 with different thicknesses of 0.26, 1.29, and 2.60 μm. Although thickness control was effective above 1 μm thick to fabricate pinhole-free roll-printed film (fig. S13, B and C), the pinholes was observed for the submicron-thick film (fig. S13A). The source and drain electrodes were realized via additional photolithography and metal deposition. Figure 6B shows a schematic of the device structure, with a channel length and width of 20 and 500 μm, respectively. The roll-printed films maintain integrity throughout the lithographic procedure, underscoring their scalability. Figure 6 (C and D)

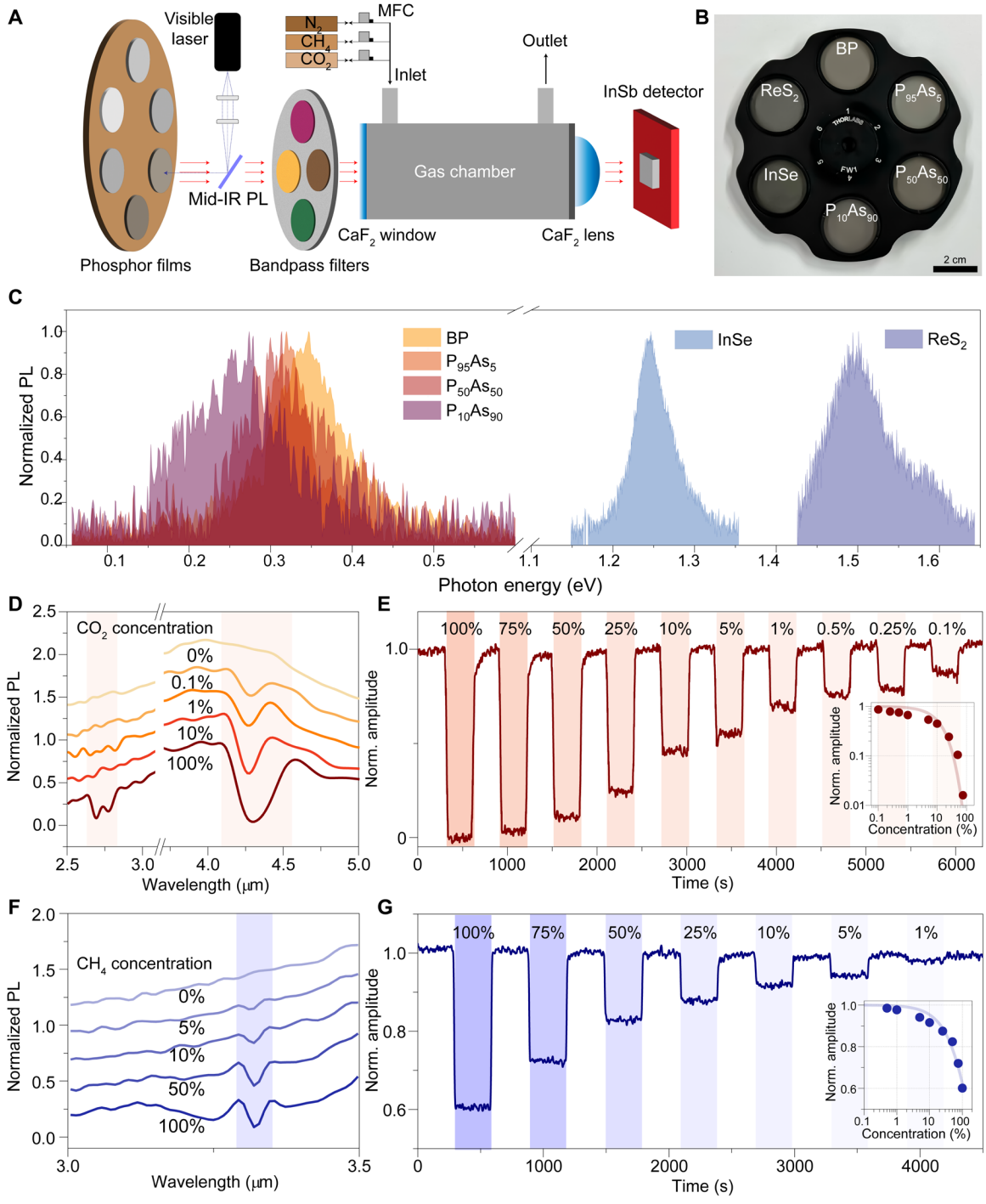

Fig. 4. NDIR gas sensing using BP and its alloy films. (**A**) Schematic diagram showing the NDIR gas-sensing system using optical phosphor films whose emission ranging from visible to mid-IR wavelength. The gas concentration and flow rate were controlled by a mass flow controllers (MFCs). (**B**) Photograph of optical phosphor wheel with different ratios of PAs alloys, InSe, and ReS_2 films. (**C**) Normalized PL spectra for optical phosphors. (**D**) PL spectra of $P_{50}As_{50}$ film with different concentrations of CO_2 gases. (**E**) Real-time CO_2 gas sensing with $P_{50}As_{50}$ optical phosphor. (**F**) PL spectra of BP film with different concentration of CH_4 gases. (**G**) Real-time CH_4 gas sensing with BP optical phosphor.

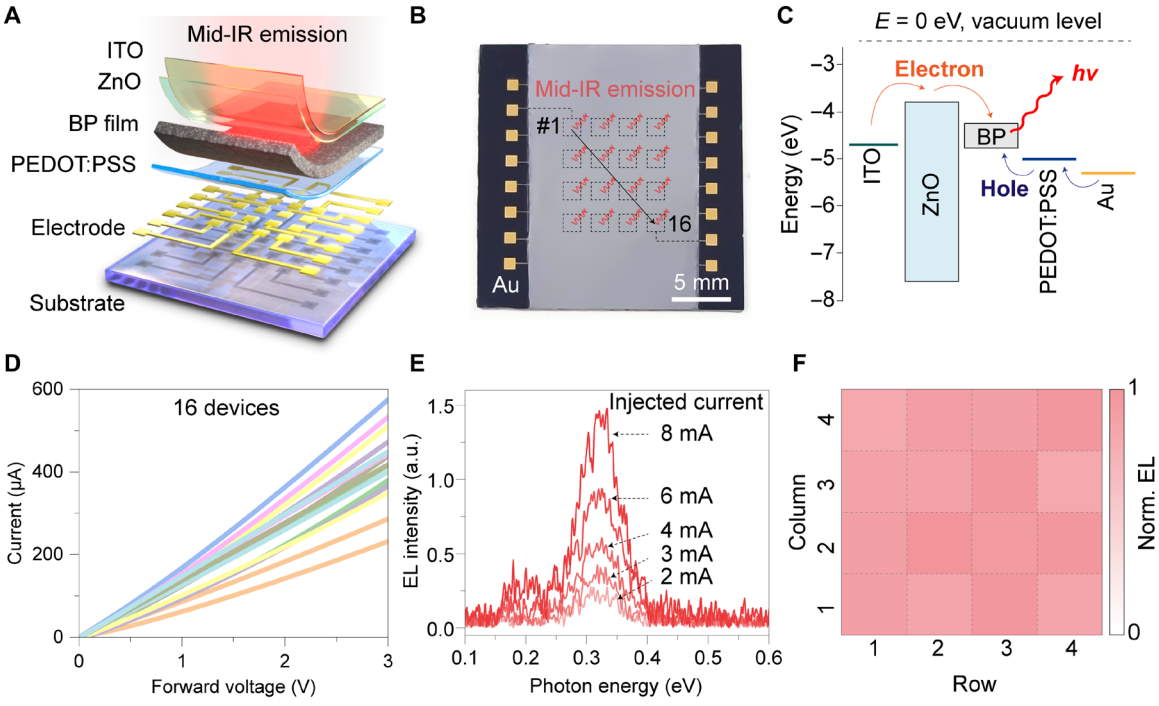

Fig. 5. Mid-IR LEDs based on heterostructure with BP film. (**A**) Schematic illustration of the structure of mid-IR LED array and (**B**) photograph of device array. The device area is 300 μm by 300 μm. (**C**) Energy band diagram of mid-IR LED. (**D**) *I-V* characteristics of the 16 LED devices. (**E**) Electroluminescence (EL) spectra (a.u., arbitrary units) from a mid-IR LED with a peak emission of 0.33 eV, operated at injection currents of 1.6 to 8.0 mA. (**F**) Mapping of EL intensities at injection current of 4 mA.

shows the typical *I-V* curves of a WS_2 field-effect transistor (FET) with n-type characteristics. The present device is turned off at $V_g = 0$ V due to the low background doping concentration of the WS_2 source used in this study. Thus, the effect of gate voltage is to turn the device on. The 5 × 5 on-chip integrated FETs exhibited similar performances. The photoresponse was characterized by illuminating the 450-nm light on the devices with a channel length of 100 μm. Figure 6E presents a time-resolved photoresponse with set drain and gate biases of 2 and 0 V, respectively. As the light intensity was augmented, the responsivity monotonically increased (Fig. 6F). Figure 6G shows a time-resolved photodetection measurement. The roll-printed WS_2 photoconductor reveals constant responsivity under the internment light exposure. We confirmed the consistent device performances regardless of normal force for rolling, as shown in fig. S14. Under a parallel white light, each pixel's performance was comparable to that of any other pixel (fig. S15A). We also demonstrated an imaging by using WS_2 sensor array under the white light through a shadow mask hollowed out in a specific shape (fig. S15, B to D). These results highlight the feasibility of integrating optoelectronic devices constructed from vdW powders, characterized by the exceptional optical quality stemming from their intrinsic self-terminated surfaces.

In conclusion, we developed a highly generic and scalable roll-printing technique for vdW thin films. Detailed characterization of the roll-printed films is performed, depicting the preservation of the high crystal and optoelectronic quality of the initial source powder. Notably, the process is performed at RT and, thus, is compatible with virtually any substrate, including low thermal budget plastics and paper. Given the simplicity of the process, the cost is dominated by that of the source powder. While the focus of the work here is on optoelectronic devices, the platform can be extended in the future for other applications, including energy storage, electromagnetic shielding, and catalysis.

MATERIALS AND METHODS

Roll printing

The bulk sources of the vdW materials, such as BP (Rasa Industries, Smart-elements), BP-As alloys, WS_2, WSe_2, MoS_2, $MoSe_2$, $MoTb_2$, SnS_2, $SnSe_2$. $ReSe_2$, ReS_2, InSe, $HfSe_2$, HfS_2, h-BN, and graphite (HQ Graphene), were first ground in a mortar and pestle to make the grain size of ~5 μm. The vdW powders (0.6 mg) were placed on the 1 cm^2 of target substrate followed by dropping 2 μl of lubricant (hexane:mineral oil = 2:1 volume ratio) (*26*, *27*). Rolling process was performed by a manual roll-printing setup consisting of the rolling rod and the stage with springs on the backside to control the normal force. A 15-cm-long stainless steel rod with a diameter of 5 mm was rolled on the stage under a normal force of 20 N, which was adjusted by the springs attached on the backside of stage (*27*). To prepare the meter-long-scale film, a longer stainless steel rod with a length of 30 cm was used. A cushion pad was placed underneath the PET film to control the normal force, instead of the metal stage with springs. The optimal rolling speed was determined to be 0.5 to 2.0 cm/s; speeds higher or lower resulted in poor film coverage or excessively thick films (>10 μm), respectively. This is probably due to increased shear forces resulting from the kinematic viscosity. The rod was rolled on the surface repeatedly, with the velocity of 0.5 to 2.0 cm/s until the entire surface was covered. Following the roll-printing process, the film underwent rinsing in a 2-propanol bath for 10 min and was then dried with nitrogen.

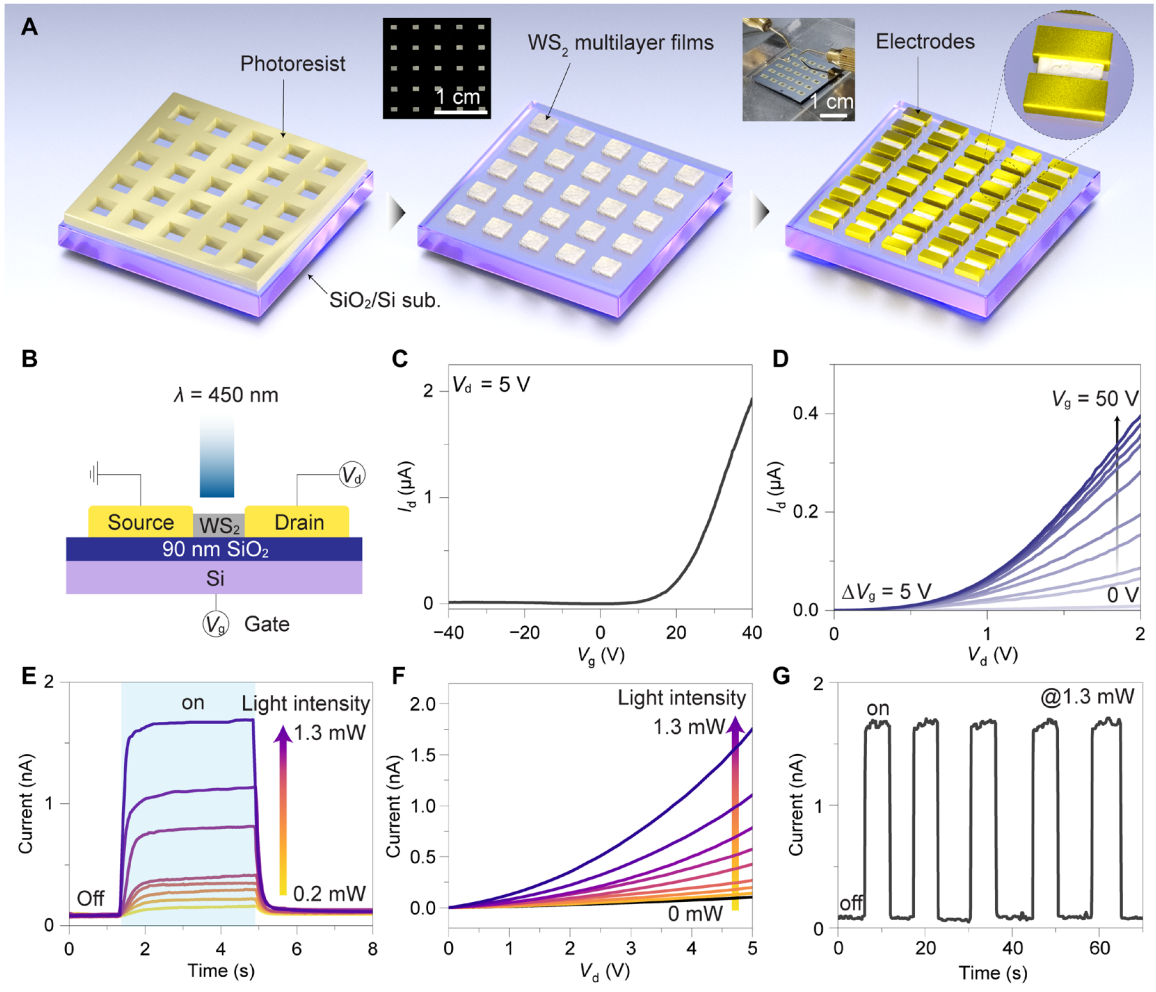

Fig. 6. Photodetection with WS_2 film array. (**A**) Schematic illustration of fabrication process of device array. A photoresist with pre-patterned window (500 μm by 500 μm) is used. After the roll-printing process and liftoff, metal electrodes are fabricated with another lithography process. Inset: Photograph of WS_2 channel array on SiO_2 substrate. (**B**) Schematic of device structure. (**C**) I_d-V_g curve of WS_2 transistor without light exposure. (**D**) I_d-V_d characteristics under different gate biases from 0 to 50 V. (**E**) Time-resolved photocurrent measurements for the WS_2 photoconductor under the intermittent light under various power intensities. The device was operated without gate bias. (**F**) Photocurrent as a function of drain voltage of the WS_2 photoconductor under the light at various power intensities. (**G**) Time-resolved photoresponse measurement under the interdigit light exposure.

Subsequently, the dried film was subjected to vacuum annealing at 100°C.

Sample preparation

The patterned CAL sample was fabricated on 100-mm 90-nm SiO_2/Si wafer. The substrate was first cleaned with acetone and 2-propanol in an ultrasonic bath for 15 min each. Then, the photolithography was performed using a direct-write tool (Heidelberg μPG 101) to pattern each letter. After the photolithography step, graphite, MoS_2, and WS_2 films were roll-printed on the C-, A-, and L-patterned areas, respectively. The printed wafer was heat-treated on the hot plate at 80°C for 10 min followed by dipping in acetone to remove the remaining photoresist.

Film characterization

XRD patterns were measured using a Rigaku SmartLab X-ray diffractometer (Cu Kα radiation) with a moving stage to obtain the mapping data. The cross-sectional images of the films and the images on the surface of steel rod were analyzed using field-emission SEM (JEOL-7610F-Plus). The XPS measurement of BP film was performed on an Axis Ultra system (Kratos, USA) with excitation by monochromatic Al Kα radiation. The height profile of roll-printed film was characterized by profilometer (Alpha-Step D-600, KLA-Tencor) and 3D Laser Confocal Microscope (LEXT OLS4000, Olympus).

Optical characterization

Raman spectra were measured by a Raman microscopic system (Horiba Labram HR Evolution) with an excitation laser (λ = 473 nm). For PL measurements in the visible wavelength, a homebuilt μ-PL instrument with Si-charge coupled device was used. Mid-IR PL spectra were measured using an FTIR spectrometer (iS50, Thermo Fisher Scientific) with a liquid N_2-cooled HgCdTe detector. As excitation light source, 514- and 638-nm lasers were used for visible and mid-IR PL measurements, respectively (*8*, *9*).

Fabrication of mid-IR LED array

A 4 × 4 mid-IR LED array was fabricated on a 90-nm SiO_2/Si substrate. After the substrate was cleaned with acetone and 2-propanol in an ultrasonic bath for 15 min each, the array of bottom electrodes was patterned by photolithography, and Ti (5 nm)/Au (30 nm) layers were deposited through electron-beam (EB) evaporation. The PEDOT:PSS (Clevios P VP AI4083) was spin-coated on the patterned electrode with 3000 rpm for 60 s followed by annealing at 100°C for 10 min. The BP film was rolled on the PEDOT:PSS film and annealed at 100°C for 30 min inside the N_2 glove box. The ZnO nanoparticle solution (Sigma-Aldrich) was spin-coated on the BP film with 3000 rpm for 60 s followed by annealing at 130°C for 10 min. The 30-nm ITO top electrode was sputtered, and contacts were created with silver paste and wire bonding.

Fabrication of WS_2 photoconductor array

A 5 × 5 WS_2 photoconductor array was fabricated on the 90-nm SiO_2/Si substrate. After the SiO_2/Si substrate was cleaned with acetone and 2-propanol in an ultrasonic bath for 15 min each, the WS_2 was roll-printed on the pre-patterned photoresist, made by conventional photolithography process. The WS_2 film was annealed at 100°C for 30 min followed by liftoff process inside the acetone bath to get the patterned WS_2 channel array. The Ti (5 nm)/Au (100 nm) source/drain electrode array was deposited via EB evaporation onto the patterned photoresist, fabricated by another photolithography step. Following the deposition, a liftoff process inside the acetone bath was conducted.

Device characterization

The EL spectra of mid-IR LED array were measured using a cryostat, equipped with a calcium fluoride (CaF_2) window. The cryostat was evacuated to a base pressure below 10^{-5} torr before the measurement. Each LED's Ti/Au bottom electrode and the shared top ITO electrode were precisely connected via wire bonding to electrode pads on a chip carrier within the cryostat. To measure the emitted mid-IR spectrum, a reflective objective with ×15 magnification was placed at the auxiliary input of a FTIR spectrometer (model iS50, Thermo Fisher Scientific), which captured the emitted mid-IR signal and directed it into the spectrometer. This spectrometer featured a CaF_2 beam splitter and a mercury cadmium telluride detector, cooled by liquid nitrogen. A forward current bias was applied using a voltage-controlled current source (model CS580, Stanford Research Systems) with a square wave form of frequency 5 kHz. The EL signal was distinguished from the thermal background through double modulation of the modulated interferogram, using a lock-in amplifier (model SR865, Stanford Research Systems) combined with a low-noise voltage preamplifier (model SR560, Stanford Research Systems). In addition, the electrical properties of the mid-IR LEDs and the WS_2 photoconductors were analyzed in a dark box using a semiconductor analyzer (model 4156C, Keysight) with a probe station. Illumination for the WS_2 photoresponse measurement was supplied by a 450-nm LED, focused onto the channel area with a microscope lens, and its power was verified using an optical power meter (model PM100D, Thorlabs).

Characterization of NDIR gas sensing

The phosphor samples, roll-printed in the plastic disk substrates, were attached to a rotating wheel. A 638-nm external laser was used to excite the vdW thin film, directing its emission into a gas chamber. Band-pass filters (full width at half maximum of 500 nm, Thorlabs) were used to specifically detect CH_4 and CO_2 at a central wavelength of 3.3 and 4.3 μm, respectively. The PL spectra with gas absorption were measured using the abovementioned FTIR system. The time-resolved NDIR gas sensing was performed using a commercial InSb photodiode cooled with liquid nitrogen. The mid-IR emissions from phosphor samples were corrected thorough CaF_2 lens.

Supplementary Materials

The PDF file includes:

Figs. S1 to S15

Legends for movies S1 and S2

Other Supplementary Material for this manuscript includes the following:

Movies S1 and S2

REFERENCES AND NOTES

1. L. Liu, T. Li, L. Ma, W. Li, S. Gao, W. Sun, R. Dong, X. Zou, D. Fan, L. Shao, C. Gu, N. Dai, Z. Yu, X. Chen, X. Tu, Y. Nie, P. Wang, J. Wang, Y. Shi, X. Wang, Uniform nucleation and epitaxy of bilayer molybdenum disulfide on sapphire. *Nature* **605**, 69–75 (2022).
2. J. Zhu, J.-H. Park, S. A. Vitale, W. Ge, G. S. Jung, J. Wang, M. Mohamed, T. Zhang, M. Ashok, M. Xue, X. Zheng, Z. Wang, J. Hansryd, A. P. Chandrakasan, J. Kong, T. Palacios, Low-thermal-budget synthesis of monolayer molybdenum disulfide for silicon back-end-of-line integration on a 200 mm platform. *Nat. Nanotechnol.* **18**, 456–463 (2023).
3. K. Kang, K.-H. Lee, Y. Han, H. Gao, S. Xie, D. A. Muller, J. Park, Layer-by-layer assembly of two-dimensional materials into wafer-scale heterostructures. *Nature* **550**, 229–233 (2017).
4. J. Shim, S.-H. Bae, W. Kong, D. Lee, K. Qiao, D. Nezich, Y. J. Park, R. Zhao, S. Sundaram, X. Li, H. Yeon, C. Choi, H. Kum, R. Yue, G. Zhou, Y. Ou, K. Lee, J. Moodera, X. Zhao, J.-H. Ahn, C. Hinkle, A. Ougazzaden, J. Kim, Controlled crack propagation for atomic precision handling of wafer-scale two-dimensional materials. *Science* **362**, 665–670 (2018).
5. X. Yang, J. Li, R. Song, B. Zhao, J. Tang, L. Kong, H. Huang, Z. Zhang, L. Liao, Y. Liu, X. Duan, X. Duan, Highly reproducible van der Waals integration of two-dimensional electronics on the wafer scale. *Nat. Nanotechnol.* **18**, 471–478 (2023).
6. T. Venanzi, H. Arora, S. Winnerl, A. Pashkin, P. Chava, A. Patanè, Z. D. Kovalyuk, Z. R. Kudrynskyi, K. Watanabe, T. Taniguchi, A. Erbe, M. Helm, H. Schneider, Photoluminescence dynamics in few-layer InSe. *Phys. Rev. Mater.* **4**, 044001 (2020).
7. S. Tongay, H. Sahin, C. Ko, A. Luce, W. Fan, K. Liu, J. Zhou, Y.-S. Huang, C.-H. Ho, J. Yan, D. F. Ogletree, S. Aloni, J. Ji, S. Li, J. Li, F. M. Peeters, J. Wu, Monolayer behaviour in bulk ReS_2 due to electronic and vibrational decoupling. *Nat. Commun.* **5**, 3252 (2014).
8. H. Kim, S. Z. Uddin, D.-H. Lien, M. Yeh, N. S. Azar, S. Balendhran, T. Kim, N. Gupta, Y. Rho, C. P. Grigoropoulos, K. B. Crozier, A. Javey, Actively variable-spectrum optoelectronics with black phosphorus. *Nature* **596**, 232–237 (2021).
9. N. Higashitarumizu, S. Z. Uddin, D. Weinberg, N. S. Azar, I. K. M. Reaz Rahman, V. Wang, K. B. Crozier, E. Rabani, A. Javey, Anomalous thickness dependence of photoluminescence quantum yield in black phosphorous. *Nat. Nanotechnol.* **18**, 507–513 (2023).
10. J. Bullock, M. Amani, J. Cho, Y.-Z. Chen, G. H. Ahn, V. Adinolfi, V. R. Shrestha, Y. Gao, K. B. Crozier, Y.-L. Chueh, A. Javey, Polarization-resolved black phosphorus/molybdenum disulfide mid-wave infrared photodiodes with high detectivity at room temperature. *Nat. Photonics* **12**, 601–607 (2018).
11. H. Jin, S. Xin, C. Chuang, W. Li, H. Wang, J. Zhu, H. Xie, T. Zhang, Y. Wan, Z. Qi, W. Yan, Y.-R. Lu, T.-S. Chan, X. Wu, J. B. Goodenough, H. Ji, X. Duan, Black phosphorus composites with engineered interfaces for high-rate high-capacity lithium storage. *Science* **370**, 192–197 (2020).
12. F. Shahzad, M. Alhabeb, C. B. Hatter, B. Anasori, S. Man Hong, C. M. Koo, Y. Gogotsi, Electromagnetic interference shielding with 2D transition metal carbides (MXenes). *Science* **353**, 1137–1140 (2016).
13. D. Deng, K. S. Novoselov, Q. Fu, N. Zheng, Z. Tian, X. Bao, Catalysis with two-dimensional materials and their heterostructures. *Nat. Nanotechnol.* **11**, 218–230 (2016).
14. N. Higashitarumizu, S. Tajima, J. Kim, M. Cai, A. Javey, Long operating lifetime mid-infrared LEDs based on black phosphorus. *Nat. Commun.* **14**, 4845 (2023).
15. S. B. Desai, S. R. Madhvapathy, M. Amani, D. Kiriya, M. Hettick, M. Tosun, Y. Zhou, M. Dubey, J. W. Ager III, D. Chrzan, A. Javey, Gold-mediated exfoliation of ultralarge optoelectronically-perfect monolayers. *Adv. Mater.* **28**, 4053–4058 (2016).
16. Y. Huang, Y.-H. Pan, R. Yang, L.-H. Bao, L. Meng, H.-L. Luo, Y.-Q. Cai, G.-D. Liu, W.-J. Zhao, Z. Zhou, L.-M. Wu, Z.-L. Zhu, M. Huang, L.-W. Liu, L. Liu, P. Cheng, K.-H. Wu, S.-B. Tian,

C.-Z. Gu, Y.-G. Shi, Y.-F. Guo, Z. G. Cheng, J.-P. Hu, L. Zhao, G.-H. Yang, E. Sutter, P. Sutter, Y.-L. Wang, W. Ji, X.-J. Zhou, H.-J. Gao, Universal mechanical exfoliation of large-area 2D crystals. *Nat. Commun.* **11**, 2453 (2020).
17. S. Yang, P. Zhang, A. S. Nia, X. Feng, Emerging 2D materials produced via electrochemistry. *Adv. Mater.* **32**, e1907857 (2020).
18. N. Liu, P. Kim, J. H. Kim, J. H. Ye, S. Kim, C. J. Lee, Large-area atomically thin MoS_2 nanosheets prepared using electrochemical exfoliation. *ACS Nano* **8**, 6902–6910 (2014).
19. C. Wang, Q. He, U. Halim, Y. Liu, E. Zhu, Z. Lin, H. Xiao, X. Duan, Z. Feng, R. Cheng, N. O. Weiss, G. Ye, Y.-C. Huang, H. Wu, H.-C. Cheng, I. Shakir, L. Liao, X. Chen, W. A. Goddard III, Y. Huang, X. Duan, Monolayer atomic crystal molecular superlattices. *Nature* **555**, 231–236 (2018).
20. O. Mashtalir, M. Naguib, V. N. Mochalin, Y. Dall'Agnese, M. Heon, M. W. Barsoum, Y. Gogotsi, Intercalation and delamination of layered carbides and carbonitrides. *Nat. Commun.* **4**, 1716 (2013).
21. D. McManus, S. Vranic, F. Withers, V. Sanchez-Romaguera, M. Macucci, H. Yang, R. Sorrentino, K. Parvez, S.-K. Son, G. Iannaccone, K. Kostarelos, G. Fiori, C. Casiraghi, Water-based and biocompatible 2D crystal inks for all-inkjet-printed heterostructures. *Nat. Nanotechnol.* **12**, 343–350 (2017).
22. G. Hu, L. Yang, Z. Yang, Y. Wang, X. Jin, J. Dai, Q. Wu, S. Liu, X. Zhu, X. Wang, T.-C. Wu, R. C. T. Howe, T. Albrow-Owen, L. W. T. Ng, Q. Yang, L. G. Occhipinti, R. I. Woodward, E. J. R. Kelleher, Z. Sun, X. Huang, M. Zhang, C. D. Bain, T. Hasan, A general ink formulation of 2D crystals for wafer-scale inkjet printing. *Sci. Adv.* **6**, eaba5029 (2020).
23. S. Pinilla, J. Coelho, K. Li, J. Liu, V. Nicolosi, Two-dimensional material inks. *Nat. Rev. Mater.* **7**, 717–735 (2022).
24. N. Gupta, S. Wang, N. Higashitarumizu, V. Wang, K. Lee, C. Park, A. Javey, Large-scale efficient mid-wave infrared optoelectronics based on black phosphorus ink. *Sci. Adv.* **9**, eadi9384 (2023).
25. G. Hu, T. Albrow-Owen, X. Jin, A. Ali, Y. Hu, R. C. T. Howe, K. Shehzad, Z. Yang, X. Zhu, R. I. Woodward, T.-C. Wu, H. Jussila, J.-B. Wu, P. Peng, P.-H. Tan, Z. Sun, E. J. R. Kelleher, M. Zhang, Y. Xu, T. Hasan, Black phosphorus ink formulation for inkjet printing of optoelectronics and photonics. *Nat. Commun.* **8**, 278 (2017).
26. Z. Fan, J. C. Ho, Z. A. Jacobson, R. Yerushalmi, R. L. Alley, H. Razavi, A. Javey, Wafer-scale assembly of highly ordered semiconductor nanowire arrays by contact printing. *Nano Lett.* **8**, 20–25 (2008).
27. R. Yerushalmi, Z. A. Jacobson, J. C. Ho, Z. Fan, A. Javey, Large scale, highly ordered assembly of nanowire parallel arrays by differential roll printing. *Appl. Phys. Lett.* **91**, 203104 (2007).
28. Z. Wu, Y. Lyu, Y. Zhang, R. Ding, B. Zheng, Z. Yang, S. P. Lau, X. H. Chen, J. Hao, Large-scale growth of few-layer two-dimensional black phosphorus. *Nat. Mater.* **20**, 1203–1209 (2021).
29. P. Zhao, R. Wang, D.-H. Lien, Y. Zhao, H. Kim, J. Cho, G. H. Ahn, A. Javey, Scanning probe lithography patterning of monolayer semiconductors and application in quantifying edge recombination. *Adv. Mater.* **31**, e1900136 (2019).

Acknowledgments: Roll printing, material characterization, and device fabrication and measurement were supported by the US Department of Energy, Office of Science, Office of Basic Energy Sciences, Materials Sciences and Engineering Division under contract no. DE-AC02-05Ch11231 (Electronic Materials program). The SEM and TEM imaging were performed at Yonsei University, supported by a grant of the Korea Health Technology R&D Project through the Korea Health Industry Development Institute (KHIDI), funded by the Ministry of Health and Welfare, Republic of Korea (grant no. HI19C1234). N.H. acknowledges support from JST PRESTO (JPMJPR23H7), Japan, and the Postdoctoral Fellowships for Research Abroad of Japan Society for the Promotion of Science. **Author contributions:** A.J. conceived the idea for the project and guided its execution. K.L., N.H., and A.J. designed the experimental methods. K.L. and N.H. prepared samples and performed optical and electrical measurements. S.W. conducted SEM analyses. C.K. helped with large-scale film formation and the photolithography process. C.Y.H. and M.M. performed XRD and XPS analyses. J.W.O. conducted FTIR analysis and drew illustrations in main figures. G.Z. performed TEM analysis. K.L. and N.H. wrote the paper. All authors discussed the results and provided revision comments on the paper. **Competing interests:** The authors declare that they have no competing interests. **Data and materials availability:** All data needed to evaluate the conclusions in the paper are present in the paper and/or the Supplementary Materials.

Submitted 24 April 2024
Accepted 1 August 2024
Published 6 September 2024
10.1126/sciadv.adq0655